Developing a Nowcasting Capability for X-Class Solar Flares Using VLF Radiowave Propagation Changes.

Harriet E. George[1,2], Craig J. Rodger[1], Mark A. Clilverd[3], Kathy Cresswell-Moorcock[1], James B. Brundell[1], and Neil R. Thomson[1]

[1]Department of Physics, University of Otago, Dunedin, New Zealand, [2]Department of Physics, Now at University of Helsinki, Helsinki, Finland, [3]British Antarctic Survey (UKRI-NERC), Cambridge, United Kingdom

Abstract A technique for analyzing very low frequency (VLF) radiowave signals is investigated in order to achieve rapid, real-time detection of large solar flares, through the monitoring of changes in VLF radio signal propagation conditions. The reliability of the use of VLF phase and amplitude perturbations to determine the X-ray fluxes involved during 10 large solar flare events (>X1) is examined. Linear regression analysis of signals from the NPM transmitter in Hawaii, received at Arrival Heights, Scott Base, Antarctica, over the years 2011–2015 shows that VLF phase perturbations during large solar flares have a 1.5–3 times lower mean square error when modeling the long wavelength X-ray fluxes than the equivalent short wavelength fluxes. The use of VLF amplitude observations to determine long or short wavelength X-ray flux levels have a 4–10 times higher mean square error than when using VLF phase. Normalized linear regression analysis identifies VLF phase as the most important parameter in the regression, followed by solar zenith angle at the midpoint of the propagation path, then the initial solar X-ray flux level (from 5 min before the impact of the solar flare), with F10.7 cm flux from the day beforehand providing the least important contribution. Transmitter phase measurements are more difficult to undertake than amplitude. However, networks of VLF receivers already exist which include the high quality phase capability required for such a nowcasting product. Such narrowband VLF data can be a redundant source of flare monitoring if satellite data is not available.

1. Introduction

Solar flares are the first in a sequence of space weather events that have the potential to impact societal technologies, that is, disrupting GPS, and high frequency (HF) communications, as well as industries using them, that is, emergency responders, maritime mobile services, and the aviation industry. The International Civil Aviation Organization (ICAO) identifies solar flares and solar storms as potential hazards that affect communications and navigation and could pose a radiation risk to aircraft crew and passengers (International Civil Aviation Organization, 2018). The provision of operational space weather information is a requirement for space weather centers. Early warning of solar flare-induced HF blackout occurrence, duration, and severity is a requirement for ICAO.

Solar flares are emissions of visible, ultraviolet, and X-ray energy from active regions on the surface of the Sun. Active regions are typically 10,000 to 100,000 km in size. The flares have an onset period lasting 10–100 s (Brown et al., 1981) and typically last for around 30 min, with more powerful flares lasting longer (Thomson et al., 2004). The electromagnetic radiation released in flares has wavelengths that range from 10 km (low to very low frequency radio waves) to 0.01 nm (X-rays and/or gamma rays). Traveling at the speed of light, the initial solar flare effects are felt on the Earth's dayside ionosphere before any warning systems can provide an alert (Lilensten, 2007). Immediate effects on aviation are via HF Communication, GPS/Glonass/Galileo/WAAS/EGNOS/MSAS, Satellites (Navigation/Communication), Low Frequency Communication, and Air Traffic Control facilities. An example of the impact of large solar flares occurring in September 2017 on technological systems including navigation services over Europe is described by Berdermann et al. (2018) and Redmon et al. (2018). These studies report that a large X9.3 flare caused some loss of nominal positioning accuracy for aircraft and Global Navigation Satellite System (GNSS) navigation support services.

Although there is increasing knowledge of the internal working of active regions, progress is still needed to accurately predict when a solar flare will occur and how intense the emission will be (Kontogiannis et al.,

2018). The X-rays produced from a solar flare on the Earth-facing side of the Sun directly impacts the dayside ionosphere. Following the solar flare occurrence, there can be two additional potential sources of disturbance to Earth-based technological systems: solar proton events (Ryan et al., 2000; Vlahos et al., 2019) with their potential to cause polar cap absorption of HF communications, and coronal mass ejections (Lilensten & Bornarel, 2006). There is not a straightforward relationship between the intensity of a solar flare and the severity of the solar proton events and coronal mass ejection effects that follow. However, analysis of the relationship between solar flare size and the upper envelope of energetic proton flux suggests that larger solar flares are more likely to produce more extreme societal consequences (Takahashi et al., 2016). Geostationary satellites currently monitor X-ray wavelengths for solar flare activity. Typically solar flares are classified according to their X-ray flux in the 0.1–0.8 nm wavelength range, termed the long wavelength range (XL). Classification is based on peak flux, with a logarithmically increasing flux scale using identifiers A, B, C, M, and X covering the ranges from 10^{-8} W m^{-2} upward in orders of magnitude steps. Solar flares can disrupt HF communications for several hours at a time, during the daylight hours and often occur with week-long clustering, originating from magnetically complex active regions (Sammis et al., 2000). Some large flares are also accompanied by strong radio bursts that may interfere with other radio frequencies and cause problems for satellite communication and radio navigation (GPS). Warning of solar flare-driven HF radio blackout occurrence, duration, and severity is a requirement for ICAO. Solar flares of X1 class are identified by ICAO as requiring a moderate space weather advisory of likely weak HF radio communication, while an X10 flare requires a severe advisory due to likely HF radio blackout conditions.

Forecasting of solar flare occurrence is an outstanding problem (Georgoulis, 2012; Kontogiannis et al., 2018). Predictive techniques using morphological methods based on observed parameters, such as photospheric magnetograms of solar active regions, have been developed but have low skill scores, particularly for large, infrequent flares (Barnes et al., 2016; Murray et al., 2017). In light of the difficulties in forecasting large solar flares it is imperative that a swift nowcast capability is developed, with the ability to rapidly detect, and classify enhanced solar X-ray flux levels (M. Gibbs, personal communication, 19 September 2018). At present there is a significant data latency in geostationary satellite observations with respect to the flare occurrence, that is, 2 min to process the satellite data and 4 min for the flare identification algorithm to run (Veronig et al., 2002). Nowcasting of solar flares needs to identify when a flare has occurred, when it has reached a disruptive size, when it has peaked, how large the fluxes are at the peak, and how long the flare effects will last.

Ground-based manmade transmissions of subionospheric radiowaves, in the very low frequency band (VLF, 3–30 kHz), propagate between the Earth's surface and the lower ionospheric D region at ~70 km during the day and 85 km at night (Clilverd et al., 2009). The signals have been used for many years to investigate the response of the D region to the energy deposited by solar flares (Mitra, 1974; Raulin et al., 2010; Thomson et al., 2005; Thomson & Clilverd, 2001). The X-ray fluxes from the solar flares cause excess ionization in the D region, which modifies the received amplitude and phase of otherwise stable VLF transmitters. Changes in amplitude and phase of these signals can be used as diagnostics of solar flare intensity (e.g., Pant, 1993; Thomson et al., 2004; Thomson & Clilverd, 2001), as well as studying changes in the background ionosphere as a result of variability in solar chromosphere emission levels, often proxied by F10.7 cm flux (Thomson & Clilverd, 2000).

Solar X-ray flux is too small during quiet times to significantly ionize the D region, and the daytime D region is primarily produced as a result of the ionization of nitric oxide, a minor neutral constituent, by Solar Lyman α radiation (121.6 nm). However, during solar flares X-rays are able to ionize additional constituents, including N_2 and O_2 (e.g., Banks & Kockarts, 1973). The extra ionization lowers the effective reflection height of the ionosphere for VLF waves, perturbs received VLF transmitter amplitude, and advances the phase (e.g., Mitra, 1974). Solar flare nowcasting has been undertaken previously, using VLF propagation paths oriented primarily east-west, and primarily using signal amplitude observations (Wenzel et al., 2016). Despite different solar illumination conditions occurring over long east-west propagation paths, as well as potentially complex amplitude responses during solar flares, good correlations between VLF perturbation levels and solar flare X-ray flux enhancements were found. Other, primarily north-south orientated, analysis of VLF propagation paths has shown that for daytime paths the phase advances due to solar flares (on paths longer than a few Mm) are proportional to the logarithm of the X-ray flux (McRae & Thomson,
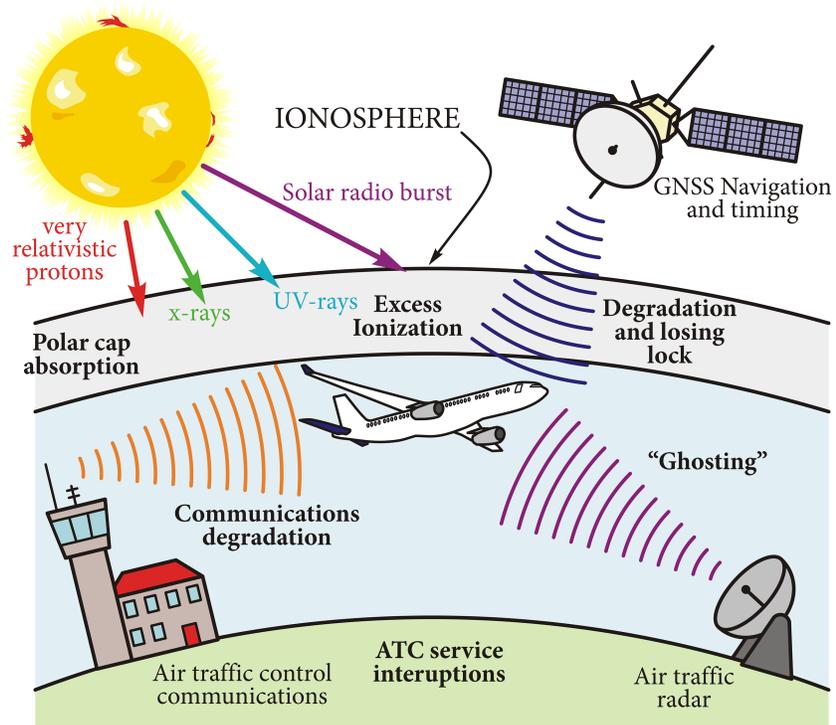
Figure 1. Illustration of effects of solar flares on the ionosphere and aviation traffic control services

2004). These D region flare-induced VLF propagation changes show no saturation effects (Thomson et al., 2005), allowing received VLF phase changes to be used for even the greatest of flares, such as the X45 super flare of 04 November 2003 (Thomson et al., 2004).

In this study we present a technique for analyzing VLF radiowave signals in order to achieve rapid, real-time detection of solar flares through changes in VLF radio signal propagation conditions. We investigate the reliability of VLF phase and amplitude perturbations, during >X1 solar flares, to determine the X-ray fluxes involved. We identify the most accurate parameterization needed to develop nowcasting equations relating VLF phase perturbations with longwave X-ray fluxes (0.1–0.8 nm, XL) and show that other relationships involving VLF amplitude perturbations, and shortwave X-ray fluxes (0.05–0.4 nm, XS), are less reliable.

2. Experimental Setup

A cartoon representation of the pathway from solar flare occurrence to impacts to users on Earth is shown in Figure 1. Solar X-ray flux generates excess ionospheric ionization over a range of altitudes from 50 to 150 km on the dayside of the Earth, simultaneously influencing HF radio communications, and satellite GPS signal quality.

In this study we analyze the phase and amplitude data from the NPM transmitter (Hawaii, 21.4 kHz, 21.4°N, 158.2°W) recorded at the field site for New Zealand's Scott Base, Arrival Heights, in Antarctica (77.8°S, 166.7°E). The path is ~11 Mm long, oriented nearly north-south, with the midpoint at 28.9°S, 164.4°W. We use the midpoint of the path to determine the solar zenith angle (SZA) during solar flares following the approach of previous studies (e.g., Cresswell-Moorcock et al., 2015; Thomson et al., 2005). Figure 2 shows a map of the Pacific region, identifying the path from the VLF transmitter in Hawaii (NPM, green circle) to Scott Base (SB, red diamond).

We made use of an extensive data set of VLF measurements made from January 2009 to June 2018. A detailed description of this data set can be found in Cresswell-Moorcock et al. (2015). Here 5 s time resolution amplitude and phase observations were analyzed for the effects of large solar flares (i.e., X-class) selected from Geostationary Operational Environmental Satellite GOES-based fluxes from the National
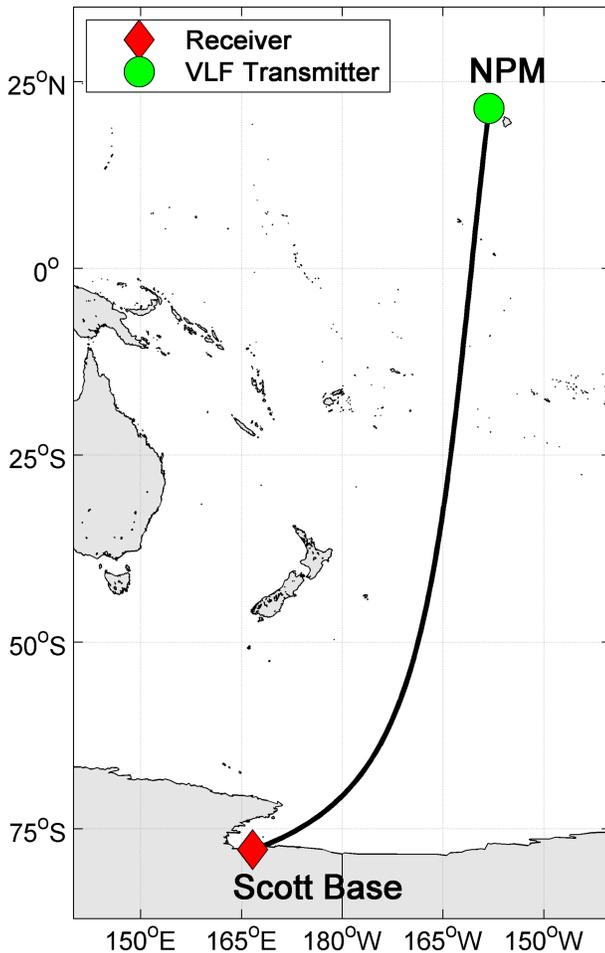
Figure 2. A map of the NPM transmitter to Scott Base receiver great circle subionospheric propagation path

Oceanic and Atmospheric Administration (NOAA) website (https://www.ngdc.noaa.gov/stp/space-weather/solar-data/solar-features/solar-flares/x-rays/goes/xrs/). The selection of X-class solar flares was limited to those flares that occurred when the VLF propagation path was sunlit and also not influenced by sunrise and sunset conditions, that is, avoiding high SZA values >85°, in order to evaluate the VLF phase/amplitude responses without the complication of large scale ionization changes that occur during sunrise and sunset conditions being included. Both transmitter and receiver had to be operating correctly at the time of the flare in order for the selected flare event to be included in the study.

Subionospheric VLF radiowave propagation conditions are modified by a solar flare through the effective lowering of the D region waveguide boundary. This occurs as a result of the excess ionization generated below the normal daytime D region altitude, caused by X-ray driven photoionization. Figure 3 shows how the phase for NPM to Scott Base was affected by a series of solar flares that occurred on 13 May 2013. The onset of sunset conditions on the path, determined by inspection of quiet day phase behavior on the days both before and after, is indicated by a vertical black line at 04 UT, while the onset of sunrise conditions is indicated by a vertical line at 15:30 UT. The phase variations (orange line, upper panel) show that the daytime phase values (18 UT to 04 UT) are advanced in comparison to the nighttime phase values (07 UT to 15 UT). There are rapidly changing transition periods during sunset (04 to 07 UT) and sunrise (15 to 18 UT). The plot also shows phase advances coincident with increases in long wavelength (XL, 0.1–0.8 nm, solid blue line) and short wavelength (XS, 0.05–0.4 nm, dashed blue line) X-ray fluxes. In the large well-defined flare event just after 02 UT, XL fluxes typically varied over ~2 orders of magnitude while the transmitter phase was perturbed by ~200°. Flares that occurred during the nighttime propagation conditions on the path did not produce any coincident changes in phase.

The lower panel of Figure 3 shows the amplitude variation during 13 May 2013 in comparison with the XL and XS fluxes. The onset of sunset and sunrise conditions is indicated by black vertical lines as in the panel above. The amplitude behavior is more variable than the phase, although the large flare at ~02 UT generates a well-defined ~10 dB of amplitude increase and a slow recovery. An increase in amplitude at ~16 UT occurs shortly after the XL and XS fluxes show a large increase. However, the amplitude variations from 16 to 19 UT are consistent with the expected behavior of modal interference during sunrise conditions (e.g., Clilverd et al., 1999). This provides an example of why flares were excluded from the study when high SZA conditions occurred.

Table 1 lists the flares included for analysis in this study, showing the date, flare start and end time, NOAA-reported flare magnitude, and the SZA at the start and end of the event, calculated at the propagation path midpoint. The flare events are separated into two sections in the table. The largest group of flares form a development group of 10 flares that are used later in this study to undertake linear regression analysis using VLF subionospheric observations. A smaller test group of three flares are used to provide an independent test of the regression formulae developed in section 4. The test group were selected from the initial 13 events through identifying flares that followed within a day of a previous flare. This had the effect of declustering the flares in the development group.

Note that the start times given in Table 1 are not precisely the same as the NOAA defined flare times (https://www.ngdc.noaa.gov/stp/space-weather/solar-data/solar-features/solar-flares/X-rays/goes/xrs/goes-xrs-report_2011.txt), which are specified at 1 min time resolution. These start times formed the initial point in our analysis. For the purposes of this study we reanalyzed the ~2 s time resolution X-ray data set in order to provide more precise timing while using the same detection algorithm as NOAA (Veronig et al., 2002).

AGU
100
ADVANCING EARTH
AND SPACE SCIENCE

Space Weather

10.1029/2019SW002297
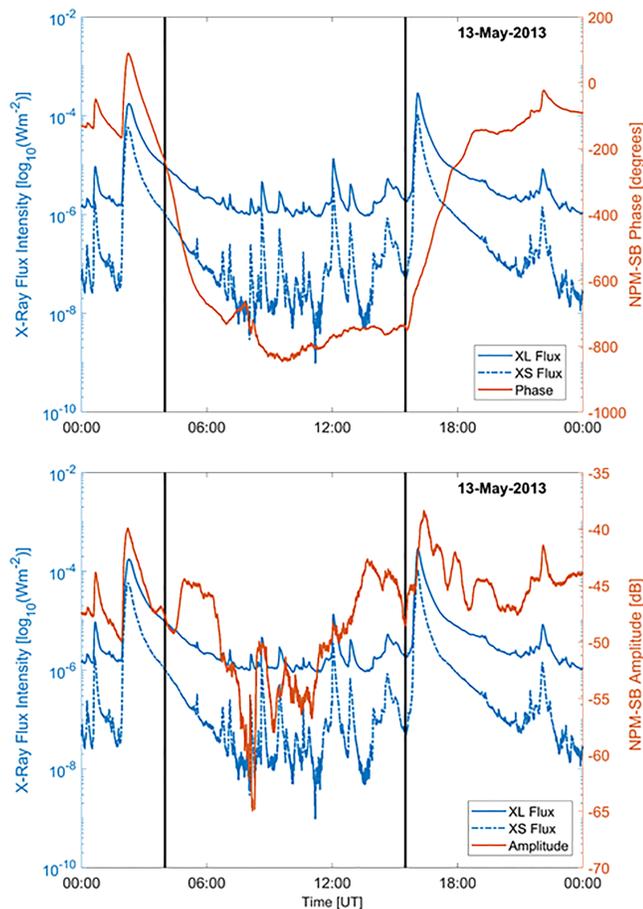
Figure 3. Example of a sequence of solar flares on 13 May 2013 (including flare E), showing variations in long wavelength X-ray flux (XL, solid blue line), short wavelength X-ray flux (XS, dashed blue line), and VLF phase and amplitude from a distant transmitter (red lines)

The flare sizes in this study range from X1.0 to X5.4, occurring between 2011 and 2015, that is, bracketing the maximum of solar cycle 24. SZA values range from 18° to 83°.

3. Linear Regression Analysis

Linear regression is a linear approach to the modeling of the relationship between a dependent variable and one or more independent, exploratory variables (Olive, 2017). We apply this approach to determine how subionospheric VLF observations can be directly linked to the magnitude of the solar flare X-ray flux striking the ionosphere. Thus, we define the dependent variable as either the long or the short wavelength solar X-ray flux, and the independent variables as either VLF phase perturbation or VLF amplitude perturbation, and SZA, F10.7 flux from the day before the flare, and initial solar X-ray flux conditions (5 min before the start time as shown in Table 1). The VLF phase or amplitude perturbation is determined by setting the phase or amplitude to zero at the start time of the flare and then measuring the induced change from that point. Table 2 summarizes the variables, indicating the symbol, and the units used.

The regression variables were selected by taking into consideration previous analysis (e.g., Cresswell-Moorcock et al., 2015; Thomson et al., 2005). Logarithmic solar X-ray flux was used in the regression analysis in order to account for its large dynamic range. As previously noted, SZA was determined for the midpoint of the propagation path, and terms for its cosine and cosine[2] were included in the regression analysis to take into account the distance through the ionosphere that the solar X-rays would have to penetrate in order to reach the D region. Daily mean F10.7 flux was taken from the day before the solar flare under study in order to have a representation of the background D region daytime ionospheric preconditioning. Preconditioning could change the size of the perturbation response because of changing modal composition of the VLF signal (Thomson & Clilverd, 2000; Cresswell-Moorcock, 2015). In the regression analysis the F10.7 flux values were expressed in SI units (SFU $\times 10^{-22}$) and a base 10 logarithm applied. The importance of the initial solar X-ray flux was investigated using two different forms. The X-ray flux 5 min prior to the start of the flare was included in one set of regressions, as this is likely to be available in a nowcasting methodology. We investigated the importance of 5 min delay to the analysis by considering a range of delays from 2 to 10 min. Very small improvements in regression performance occurred for smaller delays, but we chose 5 min in this study as representing a reasonable delay time in which to obtain X-ray flux from the satellite. Additionally, the influence of having no starting flux was also investigated; thus, the first model has five input parameters, while the other has four. In each of these cases the logarithm of the initial X-ray flux was used.

4. Results

4.1. Mean Square Error of Regression Analysis

Eight linear regression investigations were made using the development group of flares: four were compared with NOAA XL flux measurements, of which two were using VLF phase perturbations and two using VLF amplitude variations. The difference between the pairs of phase and amplitude models was the initial X-ray flux condition mentioned above, that is, either 5-min prior or no starting flux. Four other similar investigations were compared against NOAA XS flux measurements, again with two using VLF phase perturbations and two using VLF amplitude variations. In all cases the SZA and F10.7 cm flux parameters were common to

Table 1

The Flares Included for Analysis in This Study, Showing the Development and Test Groups Separately, With Their Date, Start and End Time, Flare Magnitude, and the SZA at the Start and End of the Event

Event	Date	Start time (UT)	End time (UT)	NOAA magnitude	Initial SZA (deg)	Final SZA (deg)
Development group						
A	05-May-2015	22:06:15	22:15:18	X2.7	47	46
B	24-Oct-2014	21:05:55	22:13:24	X3.1	29	18
C	20-Dec-2014	00:14:07	00:54:46	X1.8	18	27
D	13-May-2013	01:53:52	02:31:44	X1.7	65	71
E	15-May-2013	01:20:49	01:58:23	X1.2	60	65
F	28-Oct-2013	01:39:22	02:12:42	X1.0	45	51
G	07-Mar-2012	00:02:01	00:40:22	X5.4	27	32
H	06-Jul-2012	23:02:36	23:14:02	X1.1	51	52
I	15-Feb-2011	01:45:29	02:05:46	X2.2	39	43
J	06-Sep-2011	22:13:37	22:23:31	X2.1	37	36
Test group						
1	25-Oct-2014	16:49:29	18:19:09	X1.0	82	63
2	14-May-2013	00:59:10	01:20:01	X3.2	56	59
3	29-Oct-2013	21:43:59	22:00:43	X2.3	20	18

all combinations. Table 3 summarizes the results of the mean square analysis, where smaller values indicate the most accurate fits and a mean square error of 0 indicates perfect fit.

Three conclusions can be drawn from Table 3:

- Regressions using VLF phase measurements result in 4−10 times lower mean square errors for the fits than when using VLF amplitude.
- Regressions between VLF parameters and XL flux result in 1.5−3 times lower mean-square-errors for the fits compared with those undertaken with XS.
- The use of initial X-ray flux measurements taken prior to the flare start time result in 1.5−2 times lower mean square errors for the fits for VLF phase compared to those with no initial flux. Only a factor of 1.1 −1.2 times lower mean square error improvement is seen for VLF amplitude with the inclusion of an initial X-ray flux value.

4.2. Best Fit Regression Equations

The regression with the lowest mean-square-error was provided using VLF phase observations in combination with 5-min preflare X-ray flux starting value when used to determine the time varying XL flux—this value is highlighted in bold in the top-right hand section of Table 3. In this section we provide a formulation for this combination of parameters as found by linear regression and show the individual fits to each solar flare example given in Table 1. For completeness we also show the equivalent formulation when using VLF amplitude instead. We note that VLF amplitude measurements are technically easier to make than VLF phase, even though the corresponding formulation is considerably less accurate. The mean square error

Table 2

A Summary of the Linear Regression Variables, Indicating the Symbol, and the Units Used

Quantity	Symbol	Units	Comment
Long wavelength X-ray flux (XL)	IL	W m^{-2}	
Short wavelength X-ray flux (XS)	IS	W m^{-2}	Varies during flare
VLF phase perturbation	$\Delta\varphi$	Degrees (deg)	Varies during flare
VLF amplitude perturbation	ΔA	dB	Varies during flare
Solar zenith angle	SZA	Rad	Varies during flare
	cos (SZA)		
	cos^2(SZA)		
Previous daily F10.7 cm flux	F10.7	W m^{-2} Hz^{-1} (note this parameter is not in SFU)	Constant
Preflare long wavelength X-ray flux	IL_5	W m^{-2}	Constant
Preflare short wavelength X-ray flux	IS_5	W m^{-2}	Constant

Table 3

Mean Square Analysis of the Linear Regression of VLF Parameters Against NOAA X-ray Flux Measurements

VLF parameter	X-ray wavelength classification	No initial flux	5-min preflare flux
PHASE	XL	0.035	**0.014**
PHASE	XS	0.073	0.043
AMPLITUDE	XL	0.165	*0.120*
AMPLITUDE	XS	0.235	0.153

Note. The most accurate fit overall is highlighted in bold text, while the best fit for VLF amplitude is given in italics.

value for VLF amplitude with 5-min preflare flux is highlighted in italics in Table 3. We note again that the F10.7 cm flux is expressed in SI units not SFU.

I_L (XL) nowcast formulation using phase and IL_5

$$\log10(I_L) = -9.03 + 6.54 \times 10^{-3} \Delta\varphi - 2.64\cos(\text{SZA}) + 1.97\cos2(\text{SZA}) - 0.423\log10(\text{F10.7}) + 0.698\log10(IL_5) \quad (1)$$

I_L (XL) nowcast formulation using amplitude, and IL_5:

$$\log10(I_L) = -6.9 + 0.243 \, \Delta A - 1.05\cos(\text{SZA}) + 2.22\cos2(\text{SZA}) - 0.363\log10(\text{F10.7}) + 1.04\log10(IL_5) \quad (2)$$

Figure 4 shows the correspondence between the NOAA XL flux measurements and the best fit regression model determined using the observed VLF phase (equation (1)) for each of the 10 flares used in the development group analysis. The *x* axis is provided as time from start of flare in minutes, with each flare period offset in order to be sequentially shown. The *y* axis is the logarithm of long wavelength solar flux units in order to account for the large dynamic range of flux during solar flares. The NOAA XL flux data are shown in black, while the best fit linearly regressed VLF phase model output is shown by the blue line. The red dashed lines represent the smallest phase difference that needs to be applied to the model in order to encompass all peak flux values within the development group—this is particularly noticeable for flare B, where the peak flux value is just encompassed by the best fit line with fluxes calculated using a −45° offset to the measured phase change. The phase difference value determined by the fit at the peak of the flare (±45°) is used later in this study as an error estimate in determining individual flare XL flux using these now-casting formulations. The results shown in the plot indicate that although there are differences in the observed and calculated XL fluxes at the start of the solar flare, due to small additional terms influencing the initial flux levels input via IL_5, by the time the flux reaches about 10^{-5} W m^{-2} there is typically close agreement between the two.

Figure 5 shows the correspondence between the NOAA XL flux measurements and the best fit regression model determined using the observed VLF amplitude (equation (2)) for each of the 10 development group flares used in the analysis. The format is otherwise the same as in Figure 4. The amplitude difference value determined by the fits at the peak of the flares is ±3.5 dB. The results shown in the plot indicate that there are larger differences in the observed and calculated XL flux at the start of the solar flare than was the case for the phase analysis we showed in Figure 4. We also note here that although some flare flux variations are fairly well fit by the amplitude formula (e.g., flare C), flares with more complex temporal behavior are much less well modeled than by the equivalent VLF phase formulation shown in Figure 4 (i.e., flare G). We note that in this study it is possible that the X-class flares did not occur in isolation from lower level (<X class) flaring activity, and thus, some of the complex behavior seen in the examples presented in Figure 4 and 5 could be due to additional flare activity.

4.3. Normalized Regression Equation

Each parameter of the best performing regression equation, that is, equation (1), was normalized (long solar X-ray flux, VLF phase, SZA, and F10.7 value), which is to say that the values of that parameter were transformed to become zero mean unit variance. Following this process, linear regression was carried out on the development group again. By normalizing these parameters, it is possible to determine their importance to the overall equation by examining the size of the corresponding coefficients. This is standard practice when undertaking linear regression analysis, and in many studies it is common to only provide the results of the regression analysis using the normalized parameters, to focus upon the relative importance of each term. In the work presented above we have not followed that common approach, to provide equations which can be used directly with the data. In the following equations, the larger the magnitude of the coefficient the more significant it is to the relationship between solar X-ray flux and VLF propagation change.

I_L (XL) normalized formulation using phase, and IL_5:
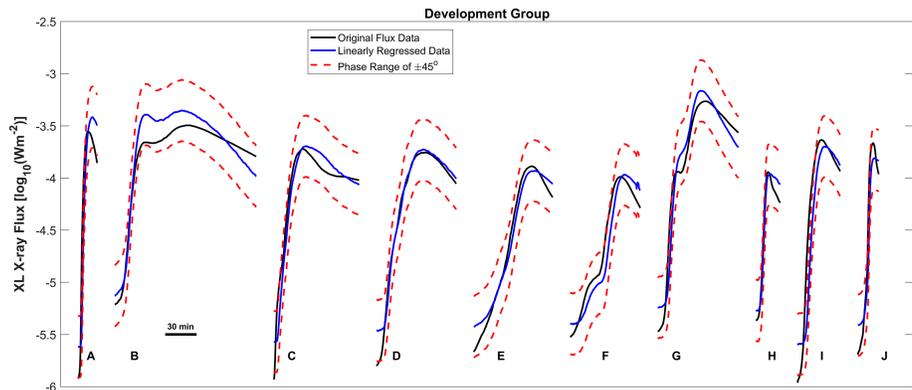
Figure 4. Best fit regression model output (blue line) using VLF phase compared with XL flux (black line) for all 10 development group solar flare events, labeled A to J. Also shown is the range of flux output from the regression model that is generated with differences of ±45° in phase (red dashed line)

$$\log10(I_L) = 5.2 + 6.6\,\Delta\,\varphi\;-4.2\cos(\text{SZA}) + 1.5\cos2(\text{SZA}) + 0.7\log10(IL_5) - 0.1\log10(\text{F10.7}) \tag{3}$$

Equation (3) is arranged in decreasing importance of each parameter to the regression fit. As expected VLF phase is the most important parameter in the regression, followed by the SZA terms. The initial solar X-ray flux level (from 5 min beforehand) is about a factor of 10 less influential than the VLF phase, with the F10.7 cm flux from the day beforehand providing the least important contribution. This ranking is potentially explained by the fact that the least important factors are constant (see Table 2) throughout the flare event, while the most important factors vary during the flare event.

5. Determination of Flare Size During Nowcasting

In this section we apply the nowcasting formulations involving VLF phase and amplitude data without prior knowledge of the NOAA solar flare start and end times. This mimics real time application of the VLF nowcasting technique. For our study case, the start time of the solar flare was determined to be the time when the phase or amplitude had been monotonically increasing for four minutes and was at least 1.4 times its initial value. These conditions are the same as the NOAA definition for solar flare start time using solar X-ray flux (Veronig et al., 2002). The end time was taken to be the time when the phase or amplitude returned to its initial value. Knowledge of the solar X-ray flux levels from 5 min prior to the identified start time was assumed. We note here that the idea of using the NOAA identification algorithm for VLF phase and amplitude data is simplistic and takes no account of the potentially complex responses shown by VLF signals during flares (Wenzel et al., 2016). However, a common, well-known approach to flare identification is
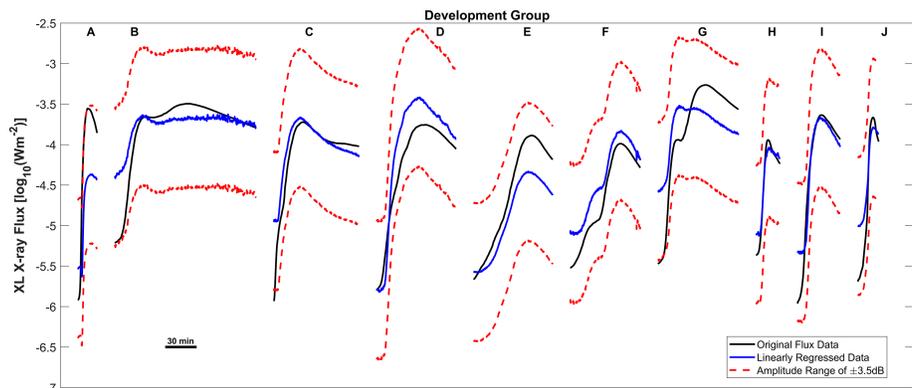
Figure 5. Same as Figure 4 but for VLF amplitude and an amplitude range of ±3.5 dB
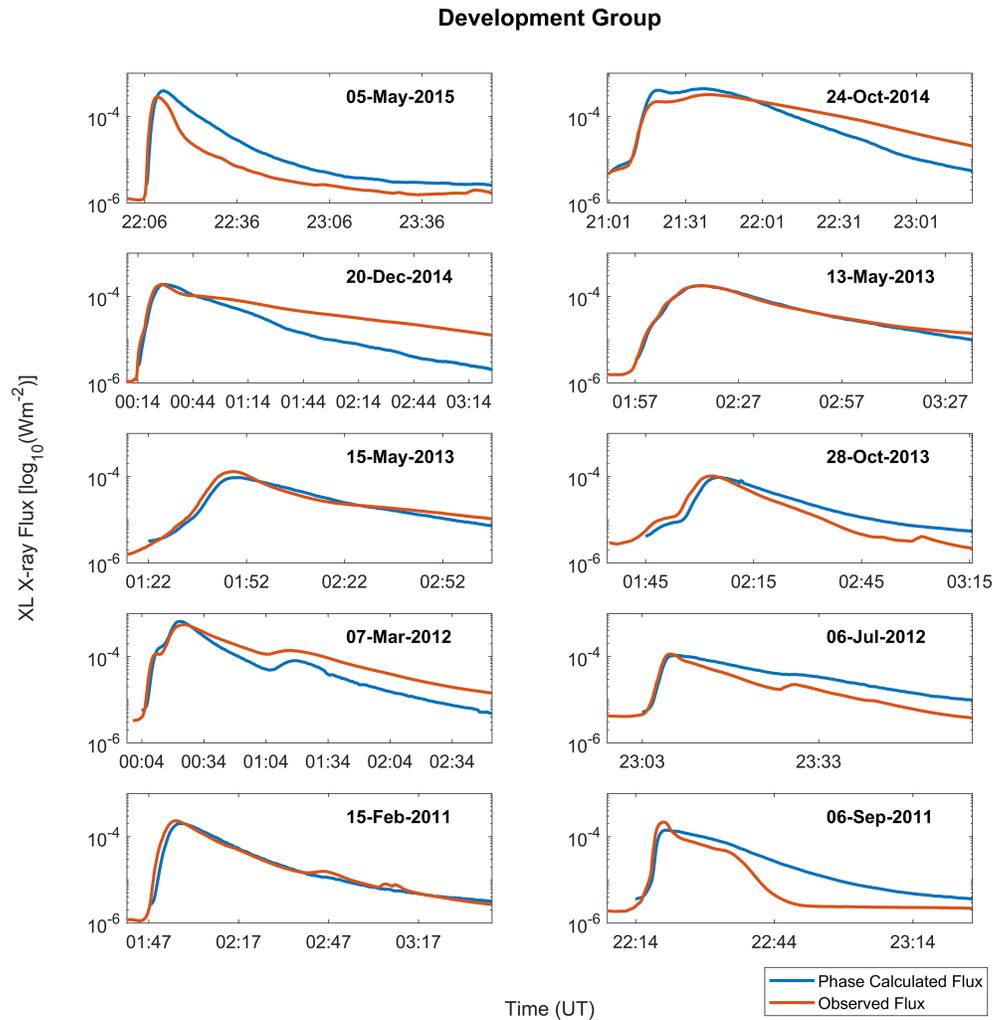
Figure 6. Nowcast XL flux calculated for all 10 development group solar flare event periods using VLF phase and calculated start time based on phase variation patterns

appropriate in this intercomparison study. Development of more responsive flare identification algorithms for VLF phase and VLF amplitude data separately will be the focus of future work.

Figure 6 shows the observed XL flux (red line) and the calculated equivalent flux using VLF phase measurements (blue line) for each of the development group solar flare events. Calculated fluxes are only plotted from the determined start of the flare event to the point where the flux perturbation returns to zero. The panels show that the initial flux values are close, and peak levels also agree reasonably well. In contrast, there is more error in the flux during the recovery phase of the flare, typically from 1 hr after the flare onset. In this figure X-ray flux is calculated from the time at which the subionospheric VLF phase data indicates that the flare has begun, rather than using the start time provided from the X-ray observations. The phase-based start times are on average only 92 s later than the X-ray-based start times. We have also plotted the observed X-ray flux prior to this phase-defined start time, and in some of the events, we see a clear onset of increasing flare fluxes before the phase determined start time. However, we note that at the start time, however it is defined, we set phase and amplitude to zero and look at the flare-induced change from that point. We also note that the postpeak disparity between GOES XL flux and XL flux from VLF phase in Figure 6 (6 September 2011 panel) could be due to underrepresentation of solar flare processes by the GOES XL flux observations at the time. The development of addition terms in the regression model, possibly a flare-based EUV contribution, is an area for future work.

Table 4
The Calculated Peak Flux From VLF Phase Compared With the NOAA Classification

Event	Date	VLF phase start time (UT)	Phase change (deg)	NOAA-based flare magnitude	VLF phase-based flare magnitude	Uncertainty range
Development group						
A	05-May-2015	22:06:59	337	X2.7	X3.9	X2.0–X7.7
B	24-Oct-2014	21:01:31	294	X3.1	X4.4	X2.2–X8.6
C	20-Dec-2014	00:14:59	290	X1.8	X1.9	M9.6–X3.7
D	13-May-2013	01:57:00	254	X1.7	X1.8	M9.0–X3.5
E	15-May-2013	01:22:21	218	X1.2	M9.4	M4.8–X1.9
F	28-Oct-2013	01:45:01	210	X1.0	M9.5	M4.8–X1.9
G	07-Mar-2012	00:04:09	319	X5.4	X6.5	X3.3–X12.7
H	06-July-2012	23:03:32	201	X1.1	X1.1	M5.4–X2.1
I	15-Feb-2011	01:47:45	291	X2.2	X2.0	X1.0–X4.0
J	06-Sep-2011	22:14:44	243	X2.1	X1.4	M7.1–X2.8
		Mean		**X2.2**	**X2.5**	**X1.3–X4.9**
Test group						
1	25-Oct-2014	16:54:51	123	X1.0	X1.4	M7.0–X2.7
2	14-May-2013	01:00:42	231	X3.2	X1.7	M9.0–X3.4
3	29-Oct-2013	21:44:35	307	X2.3	X2.7	X1.4–X5.3
		Mean		**X2.2**	**X2.0**	**X1.0–X3.8**

The calculated peak flux from VLF phase for the development group of flares is compared with the NOAA classification in Table 4 and uses the previously discussed error estimate of ±45° of phase to determine the likely range of flux uncertainty in the flare peak values. The mean of the observed and calculated peak fluxes, and the uncertainty range, are shown. The mean observed XL flux was X2.2, while the calculated value was X2.5 with an uncertainty range from X1.3 to X4.9 (i.e., a factor of ~2 larger or smaller). On average the calculated peak fluxes from VLF phase shows only a factor of 1.14 difference from the NOAA-based flare magnitude. Mean values are also given for the Test group of flares, which are discussed in the next paragraph.

Figure 7 shows the observed XL flux (red line) and the calculated equivalent flux using VLF phase measurements (blue line) for each of the test group solar flare events. For each flare the Pearson correlation coefficient, *R*, is shown. Values ranging from 0.96 to 0.99 show that the regression equations using VLF phase is well correlated with the XL flux during the flares. Table 4 also shows the calculated equivalent XL peak flux and uncertainty range for the test events. Included in the table are mean peak and uncertainty range values for both the development and test groups (shown in bold). The mean flare magnitude in the two groups according to their NOAA classification is X2.2, while the test group equivalent peak flux using VLF phase is X2.0 with an uncertainty range of a factor of 2 larger or smaller than that. Similar results were obtained with the means of the peak flux and uncertainty ranges in the development group, indicating that this level of uncertainty is representative of the regression technique using VLF phase data.

Figures 8 and 9 and Table 5 show the equivalent results when VLF amplitude is used to estimate the long wavelength X-ray flux, and also the flare start time. Figure 8 is the same format as Figure 6 and shows the amplitude results for the development group, while Figure 9 shows the results for the test group. Calculated fluxes are only plotted from the determined start of the flare event to the point where the amplitude perturbation returns to zero. In some cases this results in little coverage of the actual flare event as the amplitude perturbation is small and quickly returns to preflare levels. The flare event plotted in the panel for 5 May 2015 is a clear example of this effect. The Pearson correlation coefficients for the test group vary from
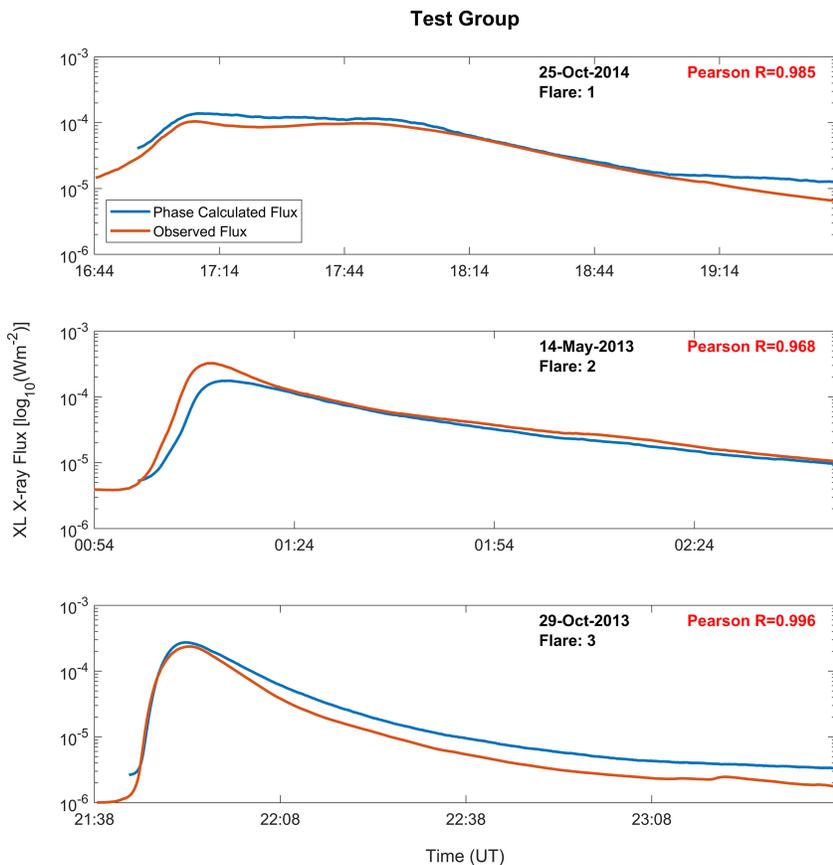
Figure 7. Nowcast XL flux calculated for the three test group solar flare event periods using VLF phase and calculated start time based on phase variation patterns. Pearson correlation coefficients are shown

0.86 to 0.98 for the regression equations using VLF amplitude. This larger range of values compared with the phase correlations is likely due to the nature of the amplitude response to solar X-ray forcing.

Table 5 is again split into development and test sections but this time for amplitude results. Compared with the phase results, there are larger ranges of uncertainty in the calculated solar flare flux magnitude in Table 5 , and this effect is also observable in Figures 8 and 9. For some flares there is almost an order of magnitude difference in the peak flux compared with the NOAA classification, which corresponds to a different magnitude class of solar flare. Included in Table 5 are mean peak and uncertainty range values for both the development and test groups (shown in bold). Once again the mean flare magnitude in the two groups according to their NOAA classification is X2.2, while the independent test group equivalent peak flux using VLF amplitude is a respectable X1.5. However, the amplitude results have an uncertainty range of a factor of 6–7 larger or smaller than that. Similar results in the development group suggest that these results are representative of the regression technique using VLF amplitude data.

Additionally, Figure 8 shows that there are events that have a large difference between the X-ray flux levels prior to the flare peak. The X-ray flux is calculated from the time at which the amplitude data indicates that the flare has begun. The start times of the flares based on X-ray flux (Table 1), VLF phase (Table 4), and VLF amplitude (Table 5) indicate that amplitude-based start times are on average 241 s later than the X-ray-based start times, while the phase times are only 92 s later than the X-ray times. This substantial delay when using the amplitude defined start time can potentially result in the 5 min preflare initial flux value being contaminated by the increased X-ray fluxes associated with the onset of the flare. Although the comparison here uses the NOAA start time algorithm, it is noted that VLF amplitude data in particular does not seem well suited to the NOAA approach and that refinement of the start time algorithm for VLF data would be beneficial.
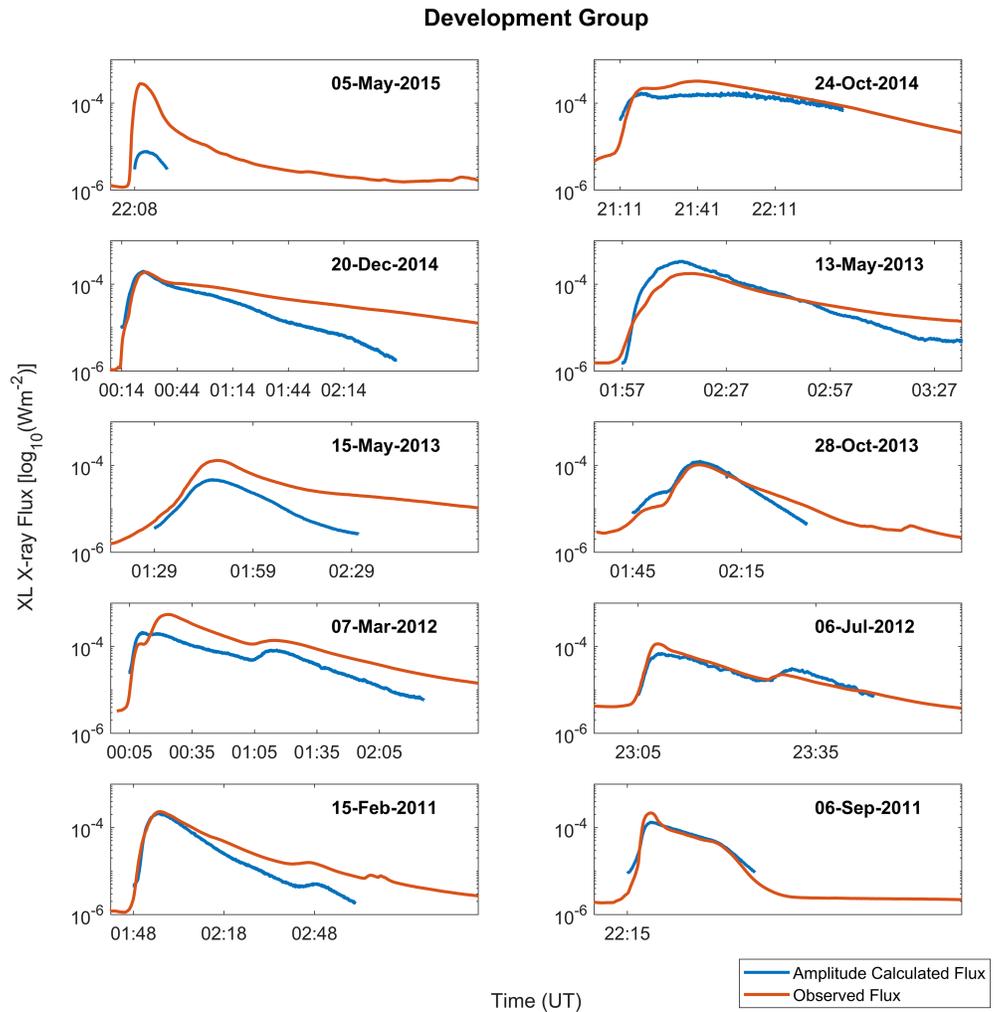
Figure 8. Same format as Figure 6 but for VLF amplitude-based formulations and with calculated start time based on amplitude variation patterns

An example of this issue is shown in the top left panel of Figure 10, an event on 5 May 2015 (which we earlier labeled as Flare A). Here the amplitude-based flare start time estimate was affected by the fact that the amplitude initially decreased at the start of the flare, and thus, the algorithm to determine the flare start time was unable to accurately identify it. The result is a late identification of the flare start time by 10 min and a poor reproduction of the subsequent observed flux variation. The difficulties of determining the flare start times from VLF observations are discussed more in the next section.

Examination of the individual panels in Figure 10 shows that although some flare X-ray flux characteristics are well reproduced by VLF amplitude-based perturbations, a substantial number are not, indicating an increased level of uncertainty when using VLF amplitude information. There is less uncertainty when using VLF phase information on well-illuminated, long paths, because lowered reflection heights lead to subionospheric phase increases (i.e., advances), due to the increased phase velocity in the waveguide.

6. Discussion

When applying the regression formulations in a nowcasting test, a technique to determine the start time of the solar flare from VLF phase or amplitude observations is required. Additionally, it is unlikely that the initial X-ray flux level will be known immediately (say within 2 min) of the start time of the flare due to operational delays in generating the fluxes. Thus we included preflare X-ray fluxes from 5 min earlier in
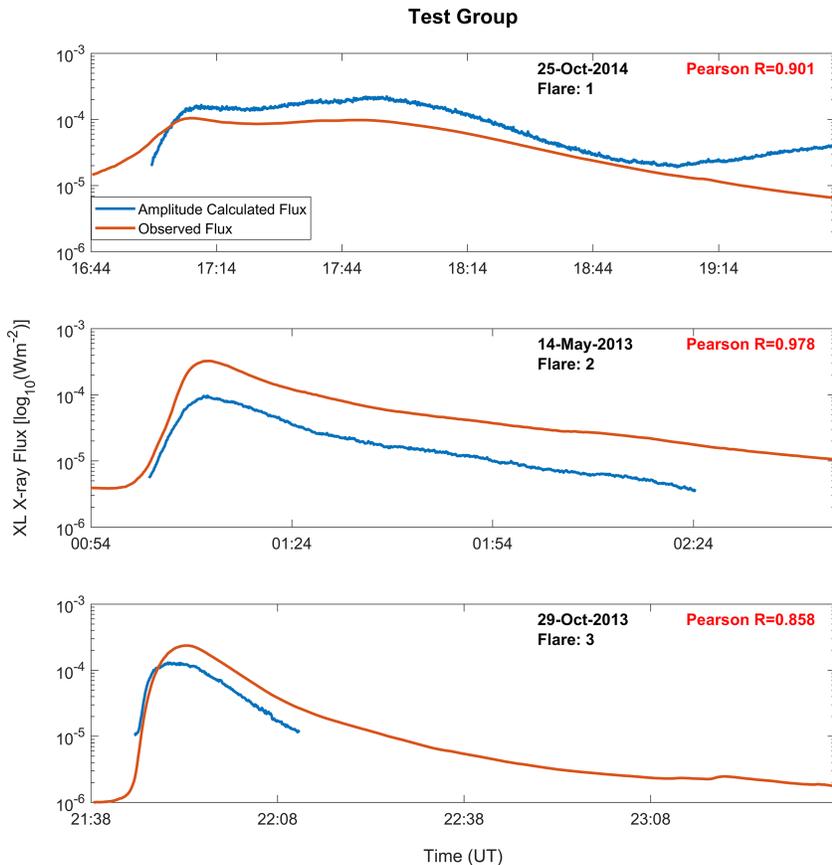
Figure 9. Same format as Figure 7 but for VLF amplitude-based formulations and with calculated start time based on amplitude variation patterns

the regression analysis and undertook the nowcasting test assuming that satellite X-ray flux measurements would be available with that level of time lag.

The flare start time algorithm adopted in this study involved looking for monotonically increasing phase or amplitude levels lasting 4 min and then noting the start time. This is similar to the technique used to determine the start time of flares from X-ray flux levels by organizations such as NOAA. In comparison to the NOAA flare start time, the VLF phase start times were on average 92 s delayed, and the amplitude start times were 241 s delayed.

As noted above, VLF phase changes during solar flares will produce a phase increase (Pant, 1993), while VLF amplitude changes can involve increases, decreases, or both (Kolarski & Grubor, 2014; Žigman et al., 2007). Even for very large flares with monotonically increasing X-ray fluxes, the amplitude need not be monotonically increasing, as seen in Figure 10 here and in Figure 10 of Thomson and Clilverd (2001). This makes the detection of the flare start time more problematic when using VLF amplitude techniques. The time delay seen for VLF amplitude detection of flares may be influenced more by the variable initial amplitude behavior, the cause of which is likely to be the combination of low levels of X-ray flux and pre-existing ionospheric conditions. When X-ray fluxes are large they completely dominate the chemistry of the D region, becoming the dominant source of ionization. However, when the solar flare fluxes are initially low, the D region is influenced by the combination of Lyman α, galactic cosmic rays, and the X-ray fluxes. In this circumstance the electron number density profile gradient with altitude can become less sharp than when X-ray fluxes dominate, resulting in increased attenuation for VLF propagation (Mitra, 1974; Wait & Spies, 1964).

Figure 10 provides examples of the onset time detection during two of the flare events where the calculated fluxes from VLF phase are significantly better than those from VLF amplitude. The first example event

Table 5
The Calculated Peak Flux From VLF Amplitude Compared With the NOAA Classification

Event	Date	VLF Amp start time (UT)	Amplitude change (dB)	NOAA-based flare magnitude	VLF Amp-based flare magnitude	Uncertainty range
Development group						
A	05-May-2015	22:08:59	1.7	X2.7	C8.0	C1.1–M5.7
B	24-Oct-2014	21:11:01	2.3	X3.1	X1.8	M2.5–X12.7
C	20-Dec-2014	00:14:59	5.4	X1.8	X2.1	M2.9–X14.6
D	13-May-2013	01:57:00	9.7	X1.7	X3.5	M4.9–X24.5
E	15-May-2013	01:29:01	4.8	X1.2	M4.9	C6.9–X3.4
F	28-Oct-2013	01:45:01	5.4	X1.0	X1.3	M1.8–X9.6
G	07-Mar-2012	00:05:59	3.8	X5.4	X2.2	M3.1–X15.5
H	06-July-2012	23:05:02	4.0	X1.1	M7.1	M1.0–X5.1
I	15-Feb-2011	01:48:00	7.0	X2.2	X2.2	M3.1–X15.6
J	06-Sep-2011	22:15:43	4.8	X2.1	X1.4	M1.9–X9.7
		Mean		**X2.2**	**X1.5**	**M2.0–X10.7**
Test group						
1	25-Oct-2014	16:59:01	4.1	X1.0	X2.3	M3.2–X16.2
2	14-May-2013	01:02:52	5.2	X3.2	M9.9	M1.4–X7.1
3	29-Oct-2013	21:46:00	4.5	X2.3	X1.4	M1.9–X9.6
		Mean		**X2.2**	**X1.5**	**M2.0–X10.6**

shown in the left-hand column is from 5 May 2015. The figure shows XL flux, VLF phase, and VLF amplitude plotted sequentially in the left-hand column with their respective onset times of the solar flare indicated by dashed vertical lines. In this well-defined solar flare event it can be seen the flare onset time is very similar when using both XL flux and VLF phase, while the VLF amplitude onset time is significantly delayed because of the initial reduction in amplitude followed by the subsequent amplitude increase. We note here that a different trigger algorithm, sensitive to negative as well as positive amplitude perturbations, would have still failed in this case as the amplitude swings rapidly from a positive gradient, to negative, and back to positive, over a period of only a few minutes, thus failing the monotonically changing requirement in the NOAA algorithm. The result of the delayed onset time determination using amplitude is that the magnitude of the amplitude perturbation throughout the flare is less than would have been the case if the start time had been closer to the XL or phase determined times, and thus the calculated flux using amplitude is lower than the actual XL fluxes (i.e., top left panel of Figure 8).

In the right-hand column of Figure 10 the XL flux, VLF phase, and VLF amplitude from 25 October 2014 are shown along with their respective determined onset times. In this flare event case there was a very gradual increase of X-ray flux at the start of the flare, and the corresponding onset times determined using both phase and amplitude data are significantly delayed (by ~5 and 10 min, respectively) relative to the XL flux time, as a result of the required factor of 1.4 increase in 4 min used as part of the detection algorithm (Veronig et al., 2002). Tables 4 and 5 show that both phase and amplitude-based X-ray flux calculations underestimate the actual XL peak flux as a result of these delayed flare start times, although the phase-based estimate was closest (M9.3 c.f. X1.0 from GOES).

As noted above, there is typically a larger time delay between the amplitude-determined solar flare time and that using phase or X-rays. The typical offset for amplitude observations compared to the X-ray start times can be as long as the ~4 min delay caused by data handling and the processing of the X-ray data to produce a solar flare start time. As such, the amplitude data approach is not just much less accurate than the phase data approach; it also offers little improvement for nowcasting, when compared with existing satellite data approaches. It may be that further effort and analysis might improve the time delay for the amplitude data approach. However, this would not improve the poor estimate of X-ray flux magnitude. In addition, it is likely that any further effort around improving the time delay in the amplitude response might also produce similar gains around the phase or X-ray data-based approaches.

While it is likely possible to identify an algorithm that works better for flare start time than the simple monotonically increasing test that we applied in this analysis, it is clear that VLF phase measurements are easier to
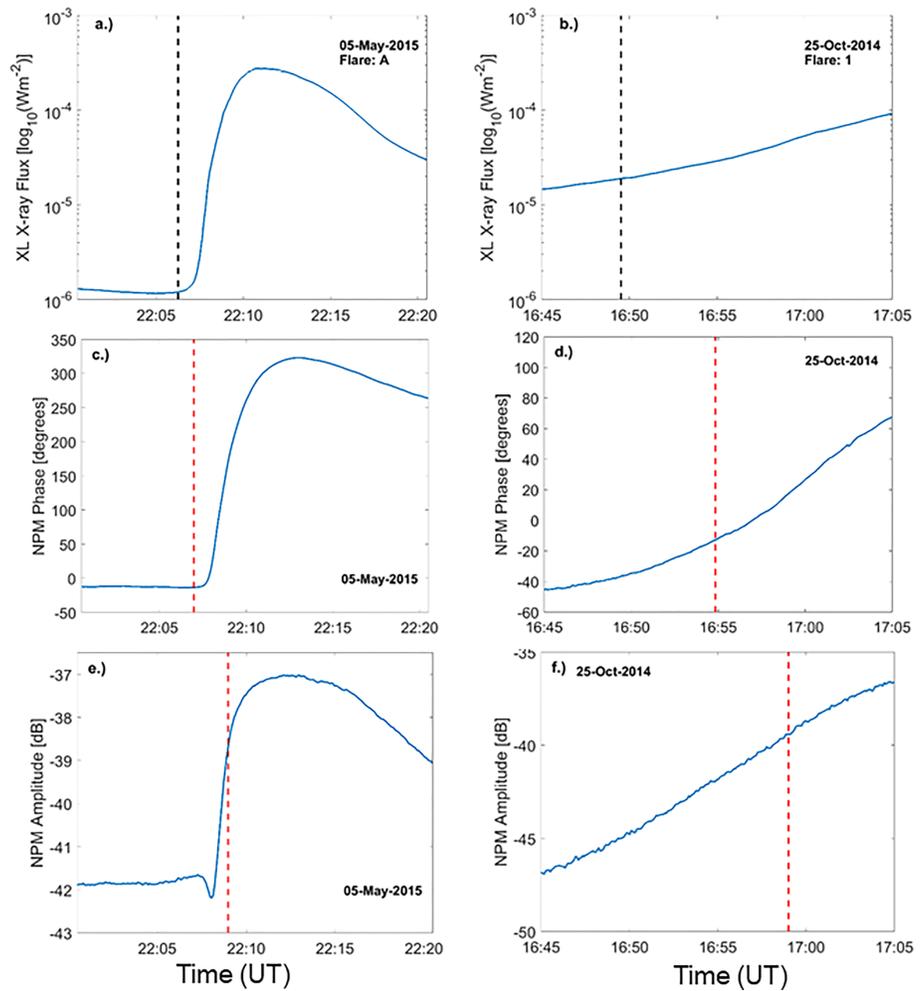
Figure 10. Examples of the variation in onset time detection using the NOAA flare detection algorithm applied to XL flux as observed by GOES, VLF phase, and VLF amplitude during solar flares on 5 May 2015 (flare A, left-hand column, panels a, c, e), and 25 October 2014 (flare 1, right-hand column, panels b, d, f)

use than VLF amplitude ones. Further, when the time of the solar flare is known accurately (as in section 4), our results show that the use of VLF phase to calculate X-ray flux levels is more reliable and has less uncertainty in its peak flux error ranges, than for VLF amplitude.

The regression equations found in this study used NPM Hawaii broadcast VLF phase and amplitude data during 10 X-class flare events recorded over a 5 year period taken from a long-running instrument at Scott Base, Antarctica. Successfully applying this technique to other transmitters and receiving sites will depend on how long the subionospheric VLF monitoring equipment has been running and whether X-class flares have occurred during the operational time. One technique may be to use smaller, more abundant flares, although there is no guarantee that the VLF response will be the same for smaller X-ray fluxes and that would need to be determined. This would be a worthwhile future study. Another possibility would be to use the U.S. Navy waveguide code, Long Wave Propagation Code (LWPC) (Ferguson & Snyder, 1990), and the ionospheric parameters H' and β (Wait & Spies, 1964), as determined by Thomson et al. (2005) for a wide range of flare sizes, to calculate (instead of measuring) the corresponding phase and amplitude changes on any proposed subionospheric path. A further approach to consider would be to express different paths and different transmitter frequencies in terms of the number of wavelengths along the propagation path and adjust the regression coefficients proportionally and then examine the quality of the linear regression analysis produced nowcasting fits. This idea was discussed briefly in Lotz and Clilverd (2019), who identified that the relationship between

peak solar flare-induced phase change versus peak X-ray flux (Thomson et al., 2005) showed the same proportionality when adjusted for the path length—expressed in wavelengths.

Measurements of VLF transmitter phase require high receiver phase stability, and signal demodulation techniques, that are more complex to undertake than straight forward amplitude measurements. However, networks of VLF receivers already exist in consortia such as AARDDVARK, SAVNET, and GIFDS (Clilverd et al., 2009; Raulin et al., 2010; Wenzel et al., 2016), which include high-quality phase capability and good internet connections required for such a nowcasting product. Ground-based VLF transmitter observations have the potential advantage of a smaller data processing latency than is experienced by satellite observations, and the X-ray product can be useful in acting as a backup measure for satellite measurement systems. Further improvements could be made by increasing the number of north-south orientated paths, and their longitudinal coverage, in order to develop a global 24/7 operational product that always undertakes observations on the dayside of the Earth.

7. Summary

Using linear regression analysis, we have investigated the most reliable technique for determining solar flare X-ray flux from distant VLF narrow-band subionospheric transmitter signals. The analysis was undertaken on a group of 10 flares that were all X1 or larger, recorded on an 11 Mm path from Hawaii to Scott Base, Antarctica, over a 5 year period around the maximum of solar cycle 24. An additional three flares were used as an independent group to test the results of the regression analysis. We have shown the following:

1. When the start time of the solar flare is known accurately, the lowest mean square error regression equation involves VLF phase, F10.7 cm flux from the day before the flare, SZA at the midpoint of the propagation path, and the X-ray flux level from 5 min prior to the flare start time.
2. The linear regression analysis equations produced using these parameters can lead to estimates of the peak X-ray flux that are within a factor of 1.14.
3. VLF phase parameters result in 1.5–3 times lower mean square errors at describing the long wavelength X-ray fluxes during a solar flare, rather than the equivalent short wavelength fluxes.
4. The use of VLF amplitude observations to determine long or short wavelength X-ray flux levels result in 4–10 times higher mean square errors than when using VLF phase.
5. Normalized linear regression analysis identified that VLF phase is the most important parameter in the regression, followed by SZA, then the initial solar X-ray flux level (from 5 min beforehand), with F10.7 cm flux from the day beforehand providing the least important contribution.
6. Nowcasting of solar X-ray flux using VLF signals requires careful analysis techniques in order to determine reliable flare start times, thereby maximizing the potential of the VLF method.

This study has shown that the use of VLF transmitter phase perturbation observations appears to be a promising approach for delivering a nowcasting product that identifies levels of X-ray flux during solar flares.

References

Banks, P. M., & Kockarts, G. (1973). *Aeronomy*. New York: Academic.

Barnes, G., Leka, K. D., Schrijver, C. J., Colak, T., Qahwaji, R., Ashamari, O. W., et al. (2016). Acomparison of flare forecasting methods I. Results from the "ALL-CLEAR" workshop. *The Astrophysical Journal*, *32*, 829–889. https://doi.org/10.3847/0004-637X/829/2/89

Berdermann, J., Kriegel, M., Banyś, D., Heymann, F., Hoque, M. M., Wilken, V., et al. (2018). Ionospheric response to the X9.3 Flare on 6 September 2017 and its implication for navigation services over Europe. *Space Weather*, *16*, 1604–1615. https://doi.org/10.1029/2018SW001933

Brown, J. C., Smith, D. F., & Spicer, D. S. (1981). Solar flare observations and their interpretations. In *The Sun as a star* (Chap. 7, pp. 181–227). NASA. Goddard Space Flight Center.

Clilverd, M. A., Rodger, C. J., Thomson, N. R., Brundell, J. B., Ulich, T., Lichtenberger, J., et al. (2009). Remote sensing space weather events: Antarctic-Arctic Radiation-belt (Dynamic) Deposition-VLF Atmospheric Research Konsortium network. *Space Weather*, *7*(4). https://doi.org/10.1029/2008SW000412

Clilverd, M. A., Thomson, N. R., & Rodger, C. J. (1999). Sunrise effects on VLF signals propagating over a long north-south path. *Radio Science*, *34*(4), 939–948. https://doi.org/10.1029/1999RS900052

Cresswell-Moorcock, K., Rodger, C. J., Clilverd, M. A., & Milling, D. K. (2015). Techniques to determine the quiet day curve for a long period of subionospheric VLF observations. *Radio Science*, *50*, 453–468. https://doi.org/10.1002/2015RS005652

Ferguson, J. A., & Snyder, F. P. (1990). *Computer programs for assessment of long wavelength radio communications, version 1.0: Full FORTRAN code user's guide. (Naval Ocean Systems Center Tech. Doc. 1773, DTIC AD-B144 839)*. Alexandria, 853 VA: Defense Technical Information Center.

Georgoulis, M. (2012). On our ability to predict major solar flares. *Astrophysics and Space Science Proceedings*, *30*, 93–116. https://doi.org/10.1007/978-3-642-29417-4

International Civil Aviation Organization (2018). *Manual on Space Weather Information in Support of International Air Navigation*, (p. 2018. Available from:). International Civil Aviation Organization Doc 10100. https://www.icao.int/airnavigation/METP/Panel%20Documents/Doc.10100.Space%20Weather%20Manual%20FINAL%20DRAFT%20Version.pdf

Kolarski, A., & Grubor, D. (2014). Sensing the Earth's low ionosphere during solar flares using VLF signals and goes solar X-ray data. *Advances in Space Research*, *53*, 1595–1602. https://doi.org/10.1016/j.asr.2014.02.022

Kontogiannis, I., Georgoulis, M. K., Park, S.-H., & Guerra, J. A. (2018). Testing and improving a set of morphological predictors of flaring activity. *Solar Physics*, *293*(6), 96–18. https://doi.org/10.1007/s11207-018-1317-2

Lilensten, J. (2007). *Space weather: Research towards applications in Europe*. Dordrecht, The Netherlands: Springer. https://doi.org/10.1007/1-4020-5446-7

Lilensten, J., & Bornarel, J. (2006). *Space weather, environment and societies*. Dordrecht, The Netherlands: Springer. https://doi.org/10.1007/1-4020-4332-5

Lotz, S. I., & Clilverd, M. A. (2019). Demonstrating the use of a class of min-max smoothers for D region event detection in narrow band VLF phase. *Radio Science*, *54*, 233–244. https://doi.org/10.1029/2018RS006701

McRae, W. M., & Thomson, N. R. (2004). Solar flare induced ionospheric D-region enhancements from VLF phase and amplitude observations. *Journal of Atmospheric and Solar - Terrestrial Physics*, *66*(1), 77–87. https://doi.org/10.1016/j.jastp.2003.09.009

Mitra, A. P. (1974). *Ionospheric effects of solar flares*. Netherlands: Springer. ISBN: 9789027704672. https://doi.org/10.1007/978-94-010-2231-6

Murray, S. A., Bingham, S., Sharpe, M., & Jackson, D. R. (2017). Flare forecasting at the Met Office Space Weather Operations Centre. *Space Weather*, *15*, 577–588. https://doi.org/10.1002/2016SW001579

Olive, D. J. (2017). *Linear regression, chapter 2, page 494*. Cham: Springer. ISBN: 978-3-319-55250-7. https://doi.org/10.1007/978-3-319-55252-1

Pant, P. (1993). Relation between VLF phase deviations and solar X-ray fluxes during solar flares. *Astrophysics and Space Science*, *209*(2), 297–306. https://doi.org/10.1007/BF00627449

Raulin, J.-P., Bertoni, F. C. P., Gavilan, H. R., Guevara-Day, W., Rodriguez, R., Fernandez, G., et al. (2010). Solar flare detection sensitivity using the South America VLF Network (SAVNET). *Journal of Geophysical Research*, *115*, A07301. https://doi.org/10.1029/2009JA015154

Redmon, R. J., Seaton, D. B., Steenburgh, R., He, J., & Rodriguez, J. V. (2018). September 2017's geoeffective space weather and impacts to Caribbean radio communications during hurricane response. *Space Weather*, *16*, 1190–1201. https://doi.org/10.1029/2018SW001897

Ryan, J. M., Lockwood, J. A., & Debrunner, H. (2000). Solar Energetic Particles. *Space Science Reviews*, *93*, 35–53. https://doi.org/10.1023/A:1026580008909

Sammis, I., Tang, F., & Zirin, H. (2000). The dependence of large flare occurrence on the magnetic structure of sunspots. *Astrophysics*, *540*, 583–587. https://doi.org/10.1086/309303

Takahashi, T., Yoshiyuki, M., & Kazunari, S. (2016). Scaling relations in coronal mass ejections and energetic proton events associated with solar superflares. *The Astrophysical Journal*, *833*, 1. https://doi.org/10.3847/2041-8205/833/1/L8

Thomson, N. R., & Clilverd, M. A. (2000). Solar cycle changes in daytime VLF subionospheric attenuation. *Journal of Atmospheric and Solar - Terrestrial Physics*, *62*(7), 601–608. https://doi.org/10.1016/S1364-6826(00)00026-2

Thomson, N. R., & Clilverd, M. A. (2001). Solar flare induced ionospheric D-region enhancements from VLF amplitude observations. *Journal of Atmospheric and Solar - Terrestrial Physics*, *63*(16), 1729–1737. https://doi.org/10.1016/S1364-6826(01)00048-7

Thomson, N. R., Rodger, C. J., & Clilverd, M. A. (2005). Large solar flares and their ionospheric D region enhancements. *Journal of Geophysical Research*, *110*, A06306. https://doi.org/10.1029/2005JA011008

Thomson, N. R., Rodger, C. J., & Dowden, R. L. (2004). Ionosphere gives size of greatest solar flare. *Geophysical Research Letters*, *31*, L06803. https://doi.org/10.1029/2003GL019345

Veronig, A., Temmer, M., Hanslmeier, A., Otruba, W., & Messerotti, M. (2002). Temporal aspects and frequency distributions of solar soft X-ray flares. *Astronomy and Astrophysics*, *382*, 1070–1080. https://doi.org/10.1051/0004-6361:20011694

Vlahos, L., Anastasiadis, A., Papaioannou, A., Kouloumvakos, A., & Isliker, H. (2019). Sources of solar energetic particles. *Philosophical Transactions of the Royal Society A.*, *377*. https://doi.org/10.1098/rsta.2018.0095

Wait, J. R., & Spies, K. P. (1964). Characteristics of the earth-ionosphere waveguide for VLF radio waves. *NBS Technical Note*, *300*.

Wenzel, D., Jakowski, N., Berdermann, J., Mayer, C., Valladares, C., & Heber, B. (2016). Global Ionospheric Flare Detection System (GIFDS). *Journal of Atmospheric and Solar-Terrestrial Physics*, *138*–*139*, 233–242. https://doi.org/10.1016/j.jastp.2015.12.011

Žigman, V., Grubor, D., & Šulić, D. (2007). D-region electron density evaluated from VLF amplitude time delay during X-ray solar flares. *Journal of Atmospheric and Solar-Terrestrial Physics*, *69*, 775–792. https://doi.org/10.1016/j.jastp.2007.01.012